Supplementary Information for "The Spontaneous Symmetry Breaking in Ta_2NiSe_5 is Structural in Nature"

Edoardo Baldini[a], Alfred Zong[a], Dongsung Choi[b], Changmin Lee[a], Marios H. Michael[c], Lukas Windgaetter[d], Igor I. Mazin[e], Simone Latini[d], Doron Azoury[a], Baiqing Lv[a], Anshul Kogar[a], Yifan Su[a], Yao Wang[f], Yangfan Lu[g], Tomohiro Takayama[g,h], Hidenori Takagi[g,h], Andrew J. Millis[i,j], Angel Rubio[d,j,k], Eugene Demler[c], and Nuh Gedik[*a]

[a]Department of Physics, Massachusetts Institute of Technology, 02139 Cambridge, Massachusetts, USA; [b]Department of Electrical Engineering & Computer Science, Massachusetts Institute of Technology, 02139 Cambridge, Massachusetts, USA; [c]Department of Physics, Harvard University, 02138 Cambridge, Massachusetts, USA; [d]Max Planck Institute for the Structure and Dynamics of Matter, Hamburg, Germany; [e]Department of Physics and Astronomy and Center for Quantum Materials, George Mason University, 22030 Fairfax, Virginia, USA; [f]Department of Physics and Astronomy, Clemson University, Clemson, South Carolina 29631, USA; [g]Department of Physics, University of Tokyo, Bunkyo-ku, Tokyo 113-0033, Japan; [h]Max Planck Institute for Solid State Research, 70569 Stuttgart, Germany; [i]Department of Physics, Columbia University, New York, NY 10027, USA; [j]Center for Computational Quantum Physics, The Flatiron Institute, 162 Fifth Avenue, New York, NY 10010, USA; [k]Nano-Bio Spectroscopy Group, Departamento de Física de Materiales, Universidad del País Vasco, 20018 San Sebastían, Spain

S1. Methods

A. Sample Growth and Preparation. Single crystals of Ta_2NiSe_5 were synthesized by chemical vapor transport. Elemental powders of Ta, Ni, and Se were mixed with a stoichiometric ratio and sealed into an evacuated quartz tube ($\sim 1\times10^3$ Pa) with a small amount of I_2 as transport agent. The mixture was sintered under a temperature gradient of 950/850°C. After sintering for 1 week, needle-like single crystals grew at the cold end of the tube.

For the time- and angle-resolved photoemission (trARPES) experiments, the single crystals were directly glued on a Cu holder using Ag epoxy, in order to ensure a good thermal contact in the cryostat. For the ultrafast electron diffraction (UED) experiments, an ultramicrotome fitted with a diamond blade was used to cleave a single crystal of Ta_2NiSe_5 along the *ac* plane, producing thin flakes with an approximate dimension of 600 μm × 50 nm × 200 μm. Flakes were scooped from water onto standard transmission electron microscopy (TEM) Cu grids (300 lines/inch). The TEM grids were clamped to a Cu holder that ensures good thermal contact. Sample characterization was done by a commercial TEM (Tecnai G2 Spirit TWIN, FEI) with a 120-kV electron beam energy.

B. Time- and Angle-Resolved Photoemission Spectroscopy. The Ta_2NiSe_5 single crystals were cleaved at 10-14 K under ultra-high-vacuum conditions ($<1\times10^{-10}$ torr). Systematic trARPES data were reproduced on a total of 10 samples with two different laser schemes, choosing pump fluences that could increase the electronic temperature (T_e) well above T_C while keeping the lattice temperature (T_L) always below T_C. This pump fluence range lies below the threshold fluence observed in previous experiments, in which the system metallizes transiently (1, 2) or permanently (through a multistage phase transition) (3).

Our first trARPES scheme used a setup based on an amplified Yb:KGW laser system operating at 100 kHz (PHAROS SP-10-600-PP, Light Conversion). Details are reported in Ref. (4). In brief, the laser ouput (with pulses centered around 1.19 eV) was split into a pump and probe beams. The pump beam was directed into an optical parametric amplifier (ORPHEUS, Light Conversion) to produce a near-infrared pulse at 1.55 eV. The probe pulse was frequency tripled to 3.58 eV and directed into a hollow fiber filled with Xe gas (XUUS, KMLabs). Here, pulses centered around 10.75 eV were obtained through nonlinear conversion of the 3.58 eV beam. The resulting vacuum ultraviolet pulse was passed through a custom-built grating monochromator (McPherson OP-XCT) to minimize pulse width broadening and enhance throughput efficiency. Finally, the probe was focused onto the sample with an in-plane polarization state perpendicular to the Ta and Ni chains. The temporal resolution of the setup was 230 fs, while the energy resolution was 43 meV. The second laser scheme consisted of an amplified Ti:Sapphire system (Wyvern, KMLabs), emitting ultrashort pulses around 1.55 eV and at a repetition rate of 30 kHz. A portion of the output beam was used directly as the near-infrared pump pulse at 1.55 eV, whereas the ultraviolet probe was obtained by frequency-quadrupling the laser fundamental photon energy to 6.20 eV. The probe light polarization state was set to circular. The overall time resolution was ∼160 fs (see Section S3), while the energy resolution was 31 meV.

A time-of-flight analyzer (Scienta ARTOF 10k) was used to acquire the transient band structure of Ta_2NiSe_5 in the two-dimensional k_x-k_z plane around the Γ point of the Brillouin zone without rotating the sample or the detector. The pump beam was incident on the sample at an angle of ∼45° and its polarization could be set precisely to either S or P with respect to the incident plane. The sample was oriented such that S polarization had a pure in-plane electric field component perpendicular to the chains ($E_{in} \parallel$ c), while P polarization had an in-plane component parallel to the chains ($E_{in} \parallel$ a) and an out-of-plane component perpendicular to the sample surface ($E_{out} \parallel$ b). The position of E_F was calibrated *in situ* for each sample by acquiring the steady-state ARPES spectrum of an auxiliary Bi_2Se_3 single crystal. Finally, as Ta_2NiSe_5 is an insulating sample with a single-particle gap on the order of 200 meV, we performed a systematic dependence on the probe flux to estimate possible probe-induced band shifts. In the presented data, we kept the probe flux below 0.1 electron per probe pulse to avoid space-charge effects.

C. Ultrafast Electron Diffraction. The 1.19 eV output of an amplified Yb:KGW laser system (PHAROS SP-10-600-PP, Light Conversion) operating at 100 kHz was split into pump

and probe branches. The pump beam was focused onto the sample, while the probe beam was frequency quadrupled to 4.78 eV and focused onto a Au-coated sapphire in high vacuum ($<4\times10^{-9}$ torr) to generate photoelectrons. These electrons were accelerated to 26 kV in a dc field and focused with a solenoid before diffracting from Ta_2NiSe_5 in a transmission geometry. Diffracted electrons were incident on an Al-coated phosphor screen (P-46), whose luminescence was recorded by an intensified charge-coupled device (iCCD PI-MAX II) operating in shutter mode. To track the timescales related to phonon population and lattice heating below T_C, we ensured that the transient lattice temperature never exceeded T_C. Specifically, we kept the initial sample temperature at 77 K or 300 K and illuminated the sample with a pump fluence of 0.10 mJ/cm^2.The time resolution was 0.8 ps (see Section S3).

D. First-Principles Calculations. All *ab initio* calculations were performed using the Vienna Atomistic Simulation Package (VASP) implementing the projected augmented wave (PAW) method (5). The Density Functional Theory (DFT) structural relaxation using the vdw-opt88-PBE functional (know to correctly describe both van der Waals and regular interactions) resulted in the monoclinic structure characteristic of the low-temperature phase of Ta_2NiSe_5. The relaxation was performed on a 24×4×6 k-mesh with a 460 eV cutoff. We obtained the lattice parameters $a = 3.517$ Å, $b = 12.981$ Å, and $c = 15.777$ Å, and unit cell angles $\alpha = 90.005°$, $\beta = 90.644°$, and $\gamma = 89.948°$. This structure has a small triclinic distortion (6), but it is very close to the monoclinic one, as analyzed in the Section S8. This structure agrees, within our numerical accuracy, to the monoclinic $C2/c$ cell measured in experiments (7, 8) and in agreement with the findings of Ref. (9).

DFT band structure calculations were performed on a 16×4×4 k-mesh using the standard Perdew-Burke-Ernzerhof (PBE) exchange-correlation functional (10). Afterwards, the GW bands were calculated on top of DFT at the G_0W_0 level with a 12×4×2 k-mesh. We used a 100 eV cutoff for the calculation of the random-phase approximation (RPA) polarizability and we included 1086 conduction bands and 160 frequencies for the calculation of the screened interaction. For the analysis of the electronic temperature effect on the band structure, we performed G_0W_0 calculations with the parameters reported above on top of DFT calculation with the PBE functional. A Fermi smearing for different temperatures was set for the self-consistent cycle. This allowed us to have a depletion of the top valence bands and finite occupation of the bottom conduction bands, which in turns affected the G_0W_0 corrections as discussed in the text. The complete electronic structure analysis is given in Section S8C,D.

The computation of the phonon dispersion and eigenmodes was performed on a 4×4×3 k-mesh with a 4×2×1 supercell. The analysis of the phonon modes was performed with the *Phonopy* package (11). To analyze the effect of representative phonon modes on the electronic bands, we performed G_0W_0 calculations as described above, but with the atomic positions displaced along the phonon eigenmodes by an amount equal to $\pm\sqrt{\langle \mathbf{r}^2\rangle_{\mathrm{T=0K}}}$, with $\langle \mathbf{r}^2\rangle_{\mathrm{T=0K}}$ being the amplitude of the zero-point oscillation of this mode. Similar calculations were repeated at different temperatures. More details are provided in Section S8E,F.

S2. Transient Electronic Distribution and Lattice Temperature

A. Transient Electronic Distribution. In this section, we estimate T_e and other properties of the nonequilibrium electron distribution induced by the pump in Ta_2NiSe_5, following arguments previously given in related contexts (12, 13). Since the crystals have a thickness larger than 1 mm (i.e., orders of magnitude larger than the penetration depth of the pump pulse), we assume that there is no transmission of the pump beam through the sample. Therefore, the pump energy that is not reflected at the sample surface is absorbed. Relying on the optical properties of the material and the experimental parameters, we can estimate the absorbed fluence for every measurement performed. For example, when our pump photon energy is $\hbar\Omega_{pump} = 1.55$ eV and the light beam is polarized parallel to the material's c-axis, we have that the reflectance at 11-14 K is $R = 0.455$ (14, 15). Thus, for an incident fluence of 1.56 mJ/cm^2, the corresponding absorbed fluence is 0.85 mJ/cm^2. We can estimate the energy density absorbed to be $E_v = 65$ meV per formula unit. Since each absorbed photon creates a particle-hole pair at energy 1.55 eV, we estimate that the pump produces a density of $n_{pump} \approx 0.04$ pairs per formula unit. At the minimum fluence used in our trARPES experiments the absorbed fluence is ∼0.4 mJ/cm^2, corresponding to an energy of about 30 meV per formula unit, and for the UED experiments the absorbed fluence used is ∼0.1 mJ/cm^2 corresponding to an energy of about 7.6 meV per formula unit.

The initial dynamics is entirely within the electronic subsystem, whose energy is thus conserved. Solution of the quantum Boltzmann equation in related contexts (12) indicates that the distribution thermalizes on a very short (few fs) timescale while conserving the number of electron-hole pairs. Then, over a longer (10-50 fs) timescale, an inverse Auger process (13) downscatters a carrier from the high energy tail of the distribution thereby lowering the temperature while creating a particle-hole pair. The result of this process is an intermediate-time distribution characterized by a lower temperature and a higher density of particle-hole pairs, both determined by balancing Auger and inverse Auger processes. This distribution then loses energy to the lattice on phonon-timescales and the density also recombines at a yet slower rate both from Auger and multiphonon processes. We may estimate the density of pairs in the intermediate time state by equating the Auger up and down scattering and assuming that the energy is the same as the initial energy. Following Ref. (12), we make a dynamical mean-field-like approximation in which the momentum dependence of the scattering rate is averaged over; we also take the conduction band (CB) and valence band (VB) densities of states to be the same so that electrons and holes have the same distribution functions and, in steady-state, the same chemical potential. The amplitude for the Auger upscattering (one particle at high energy $E_1 + E_2 + E_3$) to one particle E_1 plus an across bandgap excitation of one particle at E_2 and one at E_3) is then proportional to $f(E_1 + E_2 + E_3)(1 - f(E_1))(1 - f(E_2))(1 - f(E_3))$ where f is the distribution function, while the downscattering is proportional to $f(E_1)f(E_2)f(E_3)(1 - f(E_1 + E_2 + E_3))$.

F (mJ/cm^2)	E (meV/fu)	n_{ss}	T (K)	VB edge occ
0.85 (trARPES, F_{max})	65	0.12	1600	0.75
0.40 (trARPES, F_{min})	30	0.07	1200	0.82
0.10 (UED)	7.6	0.020	700	0.92

Table S1. Energy, number of excited electrons per formula unit, temperature, and occupancy of state at VB edge for pseudoequilbrium distribution generated by electron equilibration at fluences used in experiment

Equating the up and down scattering gives

$$\begin{aligned}&\int (dk_1)(dk_2)(dk_3)\\ &[f(E_1)f(E_2)f(E_3)(1-f(E_1+E_2+E_3))] =\\ &= \int (dk_1)(dk_2)(dk_3)\\ &[f(E_1+E_2+E_3)(1-f(E_1))(1-f(E_2))(1-f(E_3))]\end{aligned} \quad [S1]$$

where (dk) is the appropriate integration measure in momentum space. We assume that the distributions are Fermi functions and that, in the presence of the gap Δ, the energy dispersion is $E = \sqrt{\varepsilon_k^2 + \Delta^2}$, and the density of states $\nu(\varepsilon) = \int (dk)\delta(\varepsilon - \varepsilon_k)$ is constant and identical for the CB and VB. We define the fugacity $\zeta = e^{\frac{\mu-\Delta}{T}}$, find the $\zeta(\beta)$ that yields the desired energy density $\mathcal{E}$ assuming $\mathcal{E} = 2\int (dk) E f(E_k)$ (the 2 is from summing over electrons and holes) and then find the β that solves Eq. S1. Using $\Delta = 0.15$ eV and a density of states per formula unit $\nu = 2/eV$, we find the results presented in Table S1.

B. Transient Lattice Temperature. In this paragraph, we estimate the maximum transient T_L that can be reached in Ta_2NiSe_5 after photoexcitation. We rely on the simple thermodynamic expression

$$Q = \int_{T_{L,in}}^{T_{L,fin}} mC(T)dT \quad [S2]$$

where Q is the absorbed heat from a single laser pulse, m is the illuminated mass, $C(T)$ is the temperature-dependent specific heat, $T_{L,in}$ is the initial equilibrium temperature and $T_{L,fin}$ is the final T_L. We calculate m through the material density $\rho = 7.72$ g/cm^3 and the illuminated sample volume V. We then rely on the temperature dependence of the heat capacity, as measured in Ref. (16). Using these thermodynamic arguments, we can comment on the highest lattice temperature reached in photoexcited Ta_2NiSe_5 under different experimental conditions.

For example, in the trARPES experiments presented in this paper, $T_{L,in} = 14$ K and the largest absorbed fluence is 0.85 mJ/cm^2; in this case, the maximum lattice temperature is $T_{L,fin} = 210$ K, i.e. well below $T_C = 328$ K. In contrast, if trARPES experiments are performed at $T_{L,in} = 100$ K with fluences in the $\sim$mJ/cm^2 range, T_L quickly rises above T_C. In this case, the system enters the high-temperature orthorhombic phase, which is semimetallic in nature. However, we also remark that the response of Ta_2NiSe_5 at such high fluences can be more complex and involve multiple metastable phases (3).

Finally, for our UED experiments, $T_{L,in}$ is either 77 K or 295 K; the calculation yields a maximum $T_{L,fin}$ of 89 K or 302 K for the absorbed fluence of 0.1 mJ/cm^2. Both values lie again below T_C.

S3. Time Resolution in the Experimental Setups

Here, we estimate the time resolution of our trARPES and UED setups. For the trARPES apparatus based on the Ti:Sapphire laser, Fig. S1 shows two temporal traces at energies of -0.16 eV (orange dots) and -0.23 eV (blue dots), referenced to E_F. The time resolution is extracted from the fast rise appearing in the temporal trace at -0.23 eV, which follows the cross-correlation between our pump and the probe pulses (17). Specifically, a value of 160 ± 30 fs is obtained by fitting the derivative of the trace at -0.23 eV around zero time delay with a Gaussian function; the temporal resolution is taken as its full-width-at-half-maximum (FWHM). Given this instrumental resolution, the rise time of the trace at -0.16 eV is therefore not resolution limited and involves a phenomenon rising with a $\sim$150 fs timescale. As such, the temporal trace reaches its minimum value around 0.3-0.4 ps. This slow response is consistent with that reported in previous trARPES transient reflectivity experiments (18–22).

For UED, we determine the temporal resolution by using a Bi film whose response to photoexcitation is known and fast (23). Tracking the evolution of the most intense Debye-Scherrer ring (Fig. S2*A*), we model the fast lattice response by an exponential function convolved with a Gaussian kernel (Fig. S2*B*). The temporal resolution of 0.8 ± 0.1 ps is taken as the fitted FWHM of the Gaussian function.

All time traces of our trARPES and UED experiments are fit with a model function composed of two exponential functions. The first captures the fast initial response and the second describes the slower relaxation dynamics. Specifically, the function is

$$\begin{aligned}f(t) \quad = \quad &\Big\{\Theta(t-t_0)\cdot\left[A_1\left(1-e^{-(t-t_0)/\tau_1}\right)+\right.\\ &\left.A_2\left(1-e^{-(t-t_0)/\tau_2}\right)\right]\Big\} * \mathcal{G}(w),\end{aligned} \quad [S3]$$

where t is the pump-probe delay time, t_0 is the time zero when the pump and probe pulses maximally overlap in time, $\Theta(\cdot)$ is the Heaviside step function, $*$ denotes convolution, and $\mathcal{G}(w)$ is a normalized Gaussian function with FWHM w, where w is the instrumental temporal resolution. The fitting parameters are t_0, $A_{1,2}$, and $\tau_{1,2}$.

S4. Energy-Momentum Dispersion

In this section, we focus on the electronic structure measured in our trARPES experiments. Figure S3 shows representative constant-energy cuts of the data acquired before photoexcitation ($t < 0$) at 11 K with a probe photon energy of 10.75 eV. These data show the VB structure in the k_x-k_z momentum space, where k_x denotes the direction parallel to the Ta and Ni chains in the orthorhombic cell and k_z the one perpendicular to the chains. The energy, referenced to E_F, at which each constant-energy map is cut is indicated in the labels. In particular, Fig. S3*A* corresponds to the upper part of the VB and exhibits an anisotropic hole-like pocket centered around the Γ point of the Brillouin zone. Increasing the binding energy

(Fig. S3$B-D$) gives access to a rich pattern of bands, in agreement with previous static ARPES data (24, 25). Therefore, our results in equilibrium are consistent with the band structure known from the literature of Ta_2NiSe_5. Similar results were obtained in the measurements with the 6.20 eV probe scheme, albeit over the narrower k_x-k_z range expected from this photon energy.

Figure S4 shows the energy distribution curves (EDCs) along k_x, as obtained from the spectra in Fig. 2A, B) before time zero and at the maximum signal response. Before time zero, we observe that the the anti-bonding VB appears around -0.175 eV and the bonding VB at -0.65 eV, in perfect agreement with previous static ARPES data on similar samples at 40 K (24, 26). Moreover, the sharpness of the spectra confirms the high quality of the probed samples. Upon photoexcitation with 1.55 eV photons, these two VBs undergo changes in their peak positions, linewidth, and intensity at all momenta. The spectral weight that accumulates all the way to the Fermi energy originates from the simultaneous broadening of both VBs. Figure S4(c) shows the energy-momentum dispersion before time zero and around the maximum signal response, as obtained from tracking the VB peak energy at different momenta in the explored range. We observe that at this time delay the VB peak is shifted slightly toward higher binding energy in the momentum region where the VB is flat, whereas no sizeable changes are detected on the wings of the band (with the M-like dispersion depending on the matrix elements at the probe photon energy). This momentum dependence demonstrates that the detected shifts are not caused by a change in the workfunction of Ta_2NiSe_5. The same effects are observed when the pump polarization is set parallel to the Ta and Ni chains. In Section S5C, we show how the intensity, width, and peak position of the VB vary as a function of time.

To probe the fingerprint of the CB, we performed a separate experiment with improved sensitivity around E_F at 11 K. This is necessary because the CB has very weak intensity due to the relatively small carrier density excited across the gap. In Fig. S5 we display the trARPES snapshots acquired during this separate measurement. The snapshot in panel A shows the data acquired before photoexcitation ($t < 0$) and $k_z = 0.0$ Å^{-1}, whereas panels $B-E$ represent an enlarged version of Fig. 2$C-F$ and are obtained at $t = 0.3$ ps after photoexcitation with an absorbed pump fluence of 0.4 mJ/cm^2. As underlined in the main text, in Fig. S5A we observe only the flattened VB around the Γ point of the Brillouin zone. Pumping out of equilibrium (Fig. S5$B-E$) leads to the appearance of an upward-dispersing CB with the characteristic W-like shape expected from band hybridization and our *ab initio* calculations in the monoclinic phase (see Fig. 4B and Section S8). As mentioned above, the VB undergoes depletion and broadening, but no distortions of its shape are found compared to the spectra before photoexcitation. This is unlike the equilibrium case above T_C, at which the gap collapses and the two bands intersect, losing their hybridized M-like and W-like shapes (25). The bottom of the CB lies around 50-75 meV above the chemical potential, indicating that the latter is pinned closer to the CB minimum than the VB maximum. The CB feature can be observed directly in the raw EDCs of Fig. S6, emerging as a dispersive Gaussian/Lorentzian oscillator. As our trARPES experiments can track the spectroscopic features of both the VB and CB, we can provide an estimate of the gap size in the range 210-250 meV. This value is consistent with the optical gap measured by ellipsometry (∼200 meV at 10 K), which is typically lower than the electronic gap (14, 16). A separate estimate (300 meV at 78 K) was provided by a scanning tunneling spectroscopy (STS) study (27); however, in Section S8D, we quantitatively explain why the gap size in this STS study is larger by noting that the STS data were obtained on a sample with a monoclinic angle $\beta = 92.5°$ (i.e., much larger than the one of 90.5°-90.6° expected in the monoclinic phase) (7, 8). As such, the STS gap increases compared to the gap of a crystal with the nominal β angle. In our trARPES data, the uncertainty provided by the energy resolution and the simultaneous presence of a photoinduced carrier density does not allow us to extrapolate an absolute value for the gap size in equilibrium conditions. We can only establish that, close to the Γ point of the Brillouin zone, the gap size lies close to the equilibrium value even if T_e is well above T_C by several hundred kelvins. This finding suggests that gap opening has a dominant (and substantial) structural nature. The consequence of this observation on the fate of the EI order parameter and its collective modes is explained in Section II of the main text.

To conclude this section, we also comment on the differences between our data and those of previous trARPES experiments reported in the literature (1, 2, 18, 22, 28–30). All previous studies were performed under different experimental conditions of temperature, fluence, repetition rate, and probe flux, and thus they provided access to different physics from that explored in our measurements. In particular, several studies analyzed the transient band structure changes of Ta_2NiSe_5 when the initial temperature is in the range 100-110 K (1, 2, 18, 28, 30). Below a threhsold fluence, a transient narrowing of the electronic gap was observed, consistent with our results (2, 18, 28, 30). Indeed, at a base temperature of 110 K, the low pump fluence is high enough to increase the electronic temperature far above T_C but too low to raise the lattice temperature above T_C; the net result is that the electronic gap does not collapse at all time delays, indicating that the phase transition cannot be electronically driven in nature. Above a threhsold pump fluence, a strong renormalization of the band structure was observed, accompanied by a putative enhancement of excitonic correlations (not observed in our data) (18) or a transition to a semimetallic phase (1, 2). Thermodynamic arguments (similar to those in Section S2) enable us to conclude that in the latter conditions (initial temperature of 100 K and absorbed pump fluences in the mJ/cm^2 range), the transient lattice temperature can largely exceed T_C. Our trARPES experiments are performed at 10 K and controlled fluence, a combination of parameters that keeps the transient lattice temperature always below T_C: this is also confirmed by the presence of coherent phonon IV, which is a distinctive signature of the low-temperature phase (unlike coherent phonons I, II, and III) (31). Finally, it is instructive to compare our data with those in Ref. (22). This study explored the physics of Ta_2NiSe_5 under similar conditions of initial sample temperature, but the higher repetition rate of the laser source provided a steady-state increase in this initial temperature, reducing the single-particle gap size. Besides this small difference, the bandgap remained open at all time delays in the spectra shown, which were taken at fluences below the threshold fluence (in agreement with our study).

S5. Origin of the Rise Time in the trARPES Data

In order to determine the origin of the rise time in the trARPES data of Fig. $3A-C$, we examined several physical processes. Relying on this analysis and on the direct observation of phonon oscillations on the rise of the response (Fig. $3D$ and Fig. S8), we conclude that the rise time is phononic in nature.

A. Screening of the Coulomb Interaction. First, we consider a scenario in which the photoexcited carrier density creates a transient conducting state that screens the electron-hole Coulomb interaction. This process is present in all materials and lies at the origin of the so-called bandgap renormalization observed in standard band semiconductors (32). In the case of a pure EI (defined as a material whose gap is solely driven by an excitonic instability), this mechanism acquires special importance: indeed, increasing $T_e \gg T_C$ is expected to cause a collapse of the excitonic gap. In the following, we investigate this scenario in detail relying on our band structure calculations (Section S8). We determine the plasma frequency ω_p (i.e., the relevant parameter governing the screening dynamics) along the three crystallographic directions as a function of the Fermi energy. We use the standard procedure of averaging the squared Fermi velocity over the Fermi surface. The result is then convoluted with the Fermi function corresponding to the T_e reached in our trARPES experiment (see Section S2). We obtain that $\omega_{p,a} = 2.07$ eV, $\omega_{p,b} = 0.28$ eV, and $\omega_{p,c} = 0.59$ eV, along the a, b, and c crystallographic axes, respectively. These values imply that the screening time τ_{scr} is on the order of 2-15 fs, which is significantly faster than the timescale discussed in this paper.

Another way to estimate τ_{scr} is through the simplified formula (33)

$$\tau_{scr} = 2\pi\sqrt{\frac{\epsilon_0\epsilon_{opt}}{e^2}\frac{m^*}{\eta n_{ph}}}, \qquad [S4]$$

where η is the quantum efficiency, n_{ph} is the photoexcited carrier density, m^* is the carrier effective mass, and ϵ_{opt} is a non-resonant dielectric constant that accounts for the background polarizability of the valence electrons (i.e., the real part of the dielectric function at optical frequencies). Substituting the relevant parameters for Ta_2NiSe_5 (14) and assuming that $\eta = 1$ yields a fluence-dependent rise time of the order of $\tau_{scr} \sim 10$ fs. These results are very robust with respect to the choice of the effective dielectric constant accounting for the material's anisotropy and the carriers' effective mass. Therefore, the estimate is in agreement with the more refined *ab initio* calculation given above and confirm that screening of the Coulomb interaction (and bandgap renormalization due to an increase of T_e) cannot explain the dominant response observed in our trARPES data.

B. Quasiparticle Avalanche Multiplication. Since a putative EI bears similarities with a superconductor, we also consider the processes typically observed in the nonequilibrium response of superconductors photoexcited with photon energies much larger than the gap size. The generally-accepted picture for describing the initial ultrafast dynamics of a superconductor involves the process of quasiparticle avalanche multiplication (34–36). In this mechanism, a photon with energy exceeding the superconducting gap creates a particle-hole pair in the material. This particle-hole pair then loses its energy very rapidly through avalanche scattering with high-energy bosons within 0.1 ps, creating a large nonequilibrium boson population in the process. A subset of bosons has an energy exceeding the superconducting gap and the condensate is depleted by absorbing energy from the hot bosonic bath. In most superconductors, the bosons have been identified as high-energy phonons, but contributions from spin excitations have also been proposed (37). The number of quasiparticles created per absorbed photon can be approximately evaluated by the ratio between the initial photon energy and the superconducting gap (34). The quasiparticles recombine again and a bottleneck establishes, with the high-energy bosons being in quasi-equilibrium with the quasiparticles. In certain parameter regimes, this phenomenon can lead to the depletion of the superconducting condensate within 0.5-1 ps, causing the slow rise of the (optical or photoemission) pump-probe response (35, 36, 38). Together with the high-energy bosons, in the avalanche multiplication also low-energy bosons are emitted. However, these do not have enough energy to contribute to the condensate vaporization.

In order for the quasiparticle avalanche multiplication to govern the rise-time of the pump-probe response, we have to assume that, after photoexcitation, hot phonons are emitted with an energy exceeding the size of the single-particle gap. In Ta_2NiSe_5, the ∼180-300 meV gap (14, 16, 27) is too large to account for a quasiparticle avalanche multiplication process, as the maximum phonon energy at the Γ point of the Brillouin zone is ∼37 meV (19, 39). Therefore, it is highly unlikely that multi-phonon excitation processes from the photogenerated electron-hole pairs can be responsible for the VB delayed response. Moreover, the direct visualization of the low-energy dynamics in the VB supports this interpretation, as the VB response time would have a characteristic scaling with fluence that is not observed in our data.

C. Phonon Occupation. In this Section, we correlate the slow rise time in the VB response to the buildup of the phonon occupation. Specifically, we disentangle the contributions of the electronic and phononic degrees of freedom to the VB renormalization and show that phonons play the most significant role in the observed dynamics. To this aim, we extract quantitative information on the time evolution of the VB response by fitting the EDCs with a phenomenological model based on a Lorentzian function and a background. To maintain high time resolution, we focus on the data measured with the 6.20 eV probe beam, shown in Fig. S7A, B for representative time delays. The time evolution of the relevant VB parameters (amplitude, FWHM, and peak position) extracted from the Lorentz fit are shown in Fig. S7$C-E$. We observe that the VB amplitude (Fig. S7C) drops upon photoexcitation with a finite rise time, reaching its minimum value around 0.4 ps and recovering with an biexponential behavior (with timescales of ∼1.7 ps and ∼20 ps). The amplitude signal measures the depletion dynamics of the VB after the arrival of the pump pulse. The delayed rise and subsequent recovery indicates that the photoexcited holes (which are initially created with a high excess energy inside the VB) cool down toward the VB edge in 0.4 ps through the emission of optical phonons and recombine

following two distinct decay processes. Therefore, we attribute the timescale of 0.4 ps to the optical phonon-mediated intraband cooling dynamics of the holes. The time evolution of the VB FWHM (Fig. S7*D*) quantifies the change of the imaginary part of the self-energy in the single-particle spectral function describing the system. Upon photoexcitation, the VB broadens almost by a factor of 2 within 0.4 ps and then relaxes to a rather constant value for tens of picoseconds. The initial rise can be ascribed to the increase in the scattering processes with the optical phonons emitted in the cooling dynamics, whereas the constant plateau is reached when acoustic phonons start to dominate the scattering processes (with the carriers lying close to the band edges and undergoing recombination). This picture is consistent with the interpretation provided to the dynamics of the VB amplitude (Fig. S7*C*). Finally, Fig. S7*E* shows the time evolution of the VB peak energy. Unlike the response of the VB amplitude and FWHM, the VB peak energy responds promptly to photoexcitation with a small increase of ∼3 meV that is complete around 0.1 ps (blue shaded area in the graph). This change is followed by a decrease of ∼8 meV, which is maximum around 0.4 ps (red shaded area in the graph). The subsequent dynamics is characterized by a long recovery. Note that the first increase is not an artifact of the fit, since it mimics the resolution-limited rise found in our raw data (see Fig. S1). We attribute this rise to the process of bandgap renormalization driven by the increase of T_e, a process that is immediate with photoexcitation and often affects the VB and CB asymmetrically (42, 43). As mentioned above, while this process is present in all semiconductors (32), it acquires particular relevance in the case of a pure EI (defined as a material in which the entire hybridization gap is excitonic in nature). In such a pure EI, under our experimental conditions, the gap would undergo complete closure within the electronic timescale set by this screening process. In contrast with this scenario, we observe that the electronic screening in Ta_2NiSe_5 is small even when $T_e \gg T_C$ (as shown in Fig. 2*A*, *B*) and for all time delays during which the carriers persist in the bands. Therefore, the fact that the gap size remains finite at all time delays even if $T_e \gg T_C$ indicates a significant contribution of the structural degrees of freedom behind gap formation in Ta_2NiSe_5. Along this line, we ascribe the second effect contributing to the gap variation (i.e. the one that is complete within 0.4 ps) to the buildup of the maximum occupation for the strongly-coupled optical phonons participating in the monoclinic distortion (which is still robust under our experimental conditions, as illustrated in Section S8B). Also this scenario finds agreement with our description of the VB amplitude (Fig. S7*C*) and FWHM (Fig. S7*D*) dynamics.

S6. Analysis of the Collective Modes in trARPES

In this Section, we discuss the features in our trARPES data that indicate that in photoexcited Ta_2NiSe_5 the crystal remains in the same ground state structure at all time delays. We focus on the four frequency components that appear in the Fourier transform of Fig. 3*E*. First, we remark that the same four coherent collective modes appear in our measurements regardless of the choice of pump polarization direction (parallel or perpendicular to the Ta and Ni chains): the only difference between the two pump polarization channels is the modes' intensity, which is stronger for light polarized perpendicular to the chains (in agreement with the results of Ref. (19)).

The four detected modes correspond to Raman-active phonons that are excited coherently via an impulsive/displacive-type generation mechanism (40). These modes have been studied with a variety of steady-state (8, 19, 20, 44) and time-resolved (19, 20, 22, 29, 45) methods. In static spontaneous Raman scattering, it was found that mode II is characterized by a very narrow lineshape in the low-temperature phase of Ta_2NiSe_5 (19), undergoes a substantial broadening as the temperature approaches T_C, and persists above T_C with renormalized linewidth (and a different symmetry). The broadening occurring close T_C is ascribed to the interaction of this phonon with a continuum of electronic states; phonon anharmonicity should not contribute to the broadening of this mode close and above T_C, as shown by inelastic X-ray scattering data (8). Pump-probe experiments have observed the apparent disappearance of this mode above T_C (19, 20). However, this feature stems from a change of symmetry (from A_g to B_{2g}) in the impulsively/displacively excited mode and the limited detection of optical probes (unlike photoemission experiments). Moreover, the damping detected in pump-probe experiments relates to the decoherence experienced by the coherent phonon mode via its decay into acoustic phonons. As such, this decoherence dynamics cannot be mapped directly into the broadening observed in spontaneous Raman scattering. All these arguments indicate that the presence of mode II in our experiments and in previous trARPES studies is not sufficient to determine the crystal structure reached by the material upon photoexcitation. In contrast to mode II, mode IV (at 3.7 THz) is a direct signature of the low-temperature crystal structure of Ta_2NiSe_5. Previous studies found that below T_C this mode lies in the vicinity of another phonon at 4.0 THz (20, 31, 44, 46–48). Both modes broaden and merge with increasing temperature and only the 4.0 THz mode persists above T_C. In conclusion, the presence of mode IV is a characteristic fingerprint of the low-temperature monoclinic structure of Ta_2NiSe_5, indicating the inhibition of the structural phase transition upon increase of T_e. This finding is expected from theoretical considerations (see Section S8B).

S7. Ultrafast Electron Diffraction

We also directly visualize the evolution of the crystal structure through UED (Fig. S9*A*, details are given in Section S1). Figure S8(b) shows a static electron diffraction pattern of Ta_2NiSe_5 in the monoclinic phase, featuring two peaks at (±2, 0, 0). In Fig. S9*C*, we track the change in the diffraction intensity upon photoexcitation. We observe a signal that can be described only with a two-exponential decay (blue line) function convoluted with a Gaussian function that accounts for the time resolution of the experiment (solid blue line in Fig. S9*C*). The diffraction intensity drops promptly and is followed by a slow evolution that marks the rise of lattice heating only after ∼1 ps. Upon accounting for the instrument response function, we find that the initial sub-ps decrease is resolution-limited and indicates the immediate emission of multiple phonons (some of which revealed by trARPES) which redistribute intensity from Bragg reflections to elsewhere in the Brillouin zone.

S8. First-Principles Calculations

In this Section, we discuss the results of our systematic *ab initio* calculations.

A. Relaxation of the Unit Cell. Starting from the orthorhombic input geometry (49, 50), we perform full structure relaxation of the lattice symmetry, cell volume, and atomic coordinates. We include van der Waals forces using the vdW-opt88-functional (51, 52) and proceed with two different structural relaxation methods: (i) by imposing the orthorhombic symmetry, representative of the high-temperature phase, and (ii) by allowing for a symmetry-free full relaxation, which results in a monoclinic cell associated with the low-temperature phase. The relaxed angles for the latter read $\alpha = 90.005°$, $\beta = 90.644°$, and $\gamma = 89.948°$. We note that the obtained monoclinic symmetry has a small triclinic distortion, with an angle $\alpha = 90.005°$. These results agree with the low-temperature structure determined experimentally, in which the β angle is between 90.53° and 90.69° (7, 8). The slight deviation of the α angle from 90° remains below the resolution of most experimental methods for structural characterization, but it has been recently observed through the quadrupolar circular photogalvanic effect (6). Finally, the lattice constants for the orthorhombic cell after relaxation are $a = 3.512$Å, $b = 12.971$Å, $c = 15.778$Å, while for the monoclinic cell are $a = 3.517$Å, $b = 12.981$Å, $c = 15.777$Å.

B. Effect of T_e on the Structural Distortion. We then use DFT to study how the low-symmetry distortion reacts to an increase in T_e by introducing a finite Fermi smearing in the Brillouin zone integrations. The results are discussed in the main text and shown in Fig. 4*A*. We observe that the electron heating does not remove the monoclinic distortion even at $T_e \gg T_C$, consistent with our experimental findings of Fig. 3*E*. The amplitude of the distortion is gradually reduced, albeit never to zero.

C. Electronic Structure at Zero Temperature. To investigate the effect of the structural distortion on the electronic structure of Ta_2NiSe_5, we perform DFT calculations for both the high-temperature orthorhombic and the low-temperature monoclinic structures. After completing the structural relaxation with the vdw-opt88-PBE functional (51, 52), we calculate the two electronic structures with the PBE functional on a 16×4×4 k-mesh. The resulting band structures are shown in Fig. S10. We observe that the material is semimetallic in the orthorhombic phase, in agreement with previous results (53). In the orthorhombic structure, the VB and CB belong to two different irreducible representations of the crystal structure and no hybridization gap can be opened. This is why, in earlier studies on Ta_2NiSe_5 (53), the VB and CB of the orthorhombic phase were shifted artificially to account for the opening of a finite gap. Here instead we show, consistent with recent works (9, 25), that performing the DFT calculations in the realistic monoclinic unit cell yields an indirect bandgap of 41 meV, since the VB and CB can lead to a finite hybridization gap in the lower-symmetry structure. Therefore, the structural phase transition alone causes bandgap opening and the material turns into a small-gap semiconductor. Moreover, already at the DFT level, the VB acquires an M-like dispersion around the Γ point of the Brillouin zone, similar to the experimental findings (25, 54). In contrast, the CB dispersion does not accurately describe the measured one. We have tested our DFT results for different Pseudopotentials and converged them with respect to the basis set (plane-waves in our case) size. Increasing the exchange and correlation contribution considered in either HSE hybrid functionals or the modified-Becke-Johnson (mBJ) functional leads to a bandgap opening only in the monoclinic unit cell. (55). In summary, our results demonstrate that the change in crystal structure alone (i.e., without the need of including more refined approximations for the electronic correlations) is sufficient to turn Ta_2NiSe_5 from a semimetal into a small-gap semiconductor.

For a more accurate description of the electronic structure, we account for many-body corrections within the G_0W_0 method (57). This level of theory neglects vertex-corrections for the self-energy and terminates after one cycle of Hedin's equations. It has been proven to refine the description of the band structures of semiconductors while being still affordable computationally (58). We perform the calculations in the monoclinic cell of Ta_2NiSe_5 using a PBE-functional calculation as a starting point. The resulting band structure is shown in Fig. 4*B* in the main text. We observe that the gap reaches a value of 90 meV, with the VB maximum and CB minimum slightly shifted along the Γ-X direction of the Brillouin zone. Further calculations with the HSE03 hybrid functional as a starting point yield a gap of 169 meV (55). Spectroscopic ellipsometry experiments showed that the optical gap size at 10 K is ∼200 meV (14, 16). STS data reported the equilibrium electronic gap to be ∼300 meV (27). However, we note that in Ref. (27) the value of the β angle is not close to 90.5°-90.6° value observed by diffraction techniques (7, 8), but it is 92.5°. To investigate the discrepancy between the reported equilibrium gaps, we iterate our *GW* calculations for different monoclinic angles and find that the quasiparticle gap becomes larger with increasing β. Relying on this trend, we can extrapolate the value of the STS gap for the monoclinic angle expected for Ta_2NiSe_5. The final extrapolated gap is 165 meV. Thus, the 90-169 meV gap estimated in our *GW* calculations for the ideal $\beta = 90.644°$ is comparable to the experimental value. Further corrections in the description of the screening and the inclusion of the electron-phonon coupling in the *GW* calculations are likely to refine the gap size to larger values. The latter is already indicated by the frozen-phonon calculations we present in Section S8F, where the most strongly-coupled mode driving the orthorhombic-to-monoclinic transition provides a 10 meV increase of the gap size. Future *GW* calculations with the explicit inclusion of the electron-phonon matrix elements (which are computationally expensive) will lead to the description of the realistic electronic structure. Regardless of the actual value of the gap, the most important (and hitherto unreported) feature obtained in our *GW* calculations is the M-like (W-like) band dispersion that the VB (CB) acquires. This aspect – not fully captured at the PBE description level of Fig. S10*B* – is relevant because this characteristic dispersion has often been quoted in the literature as the fingerprint of the EI instability. In contrast to this scenario, the *GW* method does not account for any ladder-diagrammatic effects

such as the EI order and demonstrates that the structural degrees of freedom play a crucial role in determining the M-like (W-like) band flattening. In general, when two mechanisms contribute to generating the excitation gap of a solid (e.g., structural phase transition/excitonic instability, or charge-density-wave/superconductor), the resulting gap is the Pythagorean function of the two individual gaps (i.e., the components add in quadrature). In real materials, certain deviations are possible, especially since there is not rigorous way to define the two components in a distinct manner. Our *GW* results show that the structural phase transition accounts for most of the gap opening in Ta_2NiSe_5.We remark that the *GW* approach is not aimed at explaining the ultrafast dynamics of Ta_2NiSe_5. It is a parameter-free calculation on the real material structure that can only shed light on the *equilibrium* electronic structure properties. Experimentally, a nonequilibrium approach is instead needed to disentangle the response of different degrees of freedom. The extension of our *GW* calculations to a nonequilibrium setting is a challenging task that we will explore in future works. For the present paper, we only provide an approximate treatment of photodoping and coherent phonon phenomena by considering the impact of a thermalized distribution of electron-hole pairs (Section S8D) and frozen lattice disortions (Section S8F) on the *GW* electronic structure.

D. Effect of T_e on the Electronic Structure. As anticipated in Section S5, a pure EI (where the whole gap is opened by excitonic interactions) should respond to an increase of $T_e \gg T_C$ by showing complete closure of the gap. The origin of this effect lies in the screening of the Coulomb interaction caused by the photoexcitated carrier density (and therefore by T_e). This mechanism is also present under the name of bandgap renormalization in band semiconductors (32), where the electronic structure is renormalized by the presence of a carrier population inside the bands. In this case, the bandgap typically shrinks at low carrier densities and increases at sufficiently high ones (56). In nonequilibrium experiments, bandgap renormalization manifests itself promptly with photoexcitation because it is an electronic process in nature, governed by the plasma frequency. In our experimental data, we observe that the gap size responds promptly to photoexcitation (Section S5C and Fig. S7*E*), but this effect is small compared to that caused by the structural degrees of freedom. As such, the gap size remains large at all time delays, in contrast to the scenario expected for a pure EI. In this section, we investigate theoretically how the electronic structure of the monoclinic phase changes upon an increase of T_e and quantify the strength of carrier-induced screening effects.

We perform *GW* calculations by assuming a thermalized distribution of electrons (holes) in the CB (VB), set through the Fermi-Dirac distributions for different values of T_e around a value of E_F that is determined self-consistently. Specifically, we set a Fermi smearing corresponding to different values of T_e (spanning the range 0-8000 K) at the beginning of the self-consistent DFT calculations. Afterwards, we perform G_0W_0 calculations on top of such DFT ground states. The results are shown in Fig. S11*A* for representative value of T_e.

We observe that at T_e comparable to those produced by photoexcitation in our experiments ($<$ 1160 K, see Section S2), the band structure of Ta_2NiSe_5 displays a very small modification. The most pronounced change occurs at the top of the VB, where the M-like shape is slightly released and a more flattened dispersion develops. At high momenta, no variation in the dispersion occurs. Only when $T_e > 4000$ K (i.e., for unrealistic T_e in experiments, as they lie above the damage threshold of the material), the band structure renormalizes significantly. One important effect is that the temperature-corrections are quite anisotropic and larger for the CB than the VBs. We also study how the direct bandgap of Ta_2NiSe_5 reacts to the increase in T_e (Fig. S11*B*). We see that at low values of T_e ($0 < T_e < 1160$ K), the gap shrinks by a small amount (5-27 meV). At $T_e \sim 2500$ K, the gap reaches its minimum value and at higher T_e an opposite trend starts, consistent with the well-known temperature-dependent bandgap renormalization effect of standard semiconductors (56). Finally, we remark that in our calculations the chemical potential for a given temperature is fixed by the Fermi-Dirac distribution, while in the experiments the chemical potential is pinned closer to the CB (27). By considering all these aspects, we can rationalize the prompt response of VB top observed in our trARPES experiments.

E. Phonon Energy-Momentum Dispersion. Since our experimental results point toward a substantial contribution of the lattice degrees of freedom in the phase transition of Ta_2NiSe_5, here we investigate the lattice dynamics in the material's orthorhombic and monoclinic unit cells using Density Functional Perturbation Theory (59) with the vdw-opt88-PBE functional (51, 52). The calculated phonon dispersions are displayed in Fig. S12. In the orthorhombic structure (Fig. S12*A*) we observe two phonon modes with imaginary frequency, in agreement with the results of Ref. (9). The presence of imaginary frequencies is a signature that these phonons are soft modes of the orthorhombic unit cell and drive the structural phase transformation. As expected, these two modes stabilize after full relaxation in the low-temperature structure (Fig. S12*B*), acquiring a frequency of $\sim$3.5 THz. We analyze the eigenmodes of the phonons emerging in our trARPES experiment using the *Phonopy* package (11). The phonon eigenvectors are displayed in Fig. S13 and show agreement with those analyzed previously in the literature (19). In particular, mode IV is the mode that originates from the soft phonon driving the orthorhombic-to-monoclinic transition. As such, its eigenvector involves the shear motion of the neighboring Ta chains around the Ni chain.

F. Electronic Structure in a Frozen-Phonon Unit Cell. We also analyze the effect that phonon modes I-IV have on the electronic band structure of Ta_2NiSe_5. Experimentally, first insights into this aspect are provided by the curves in Figs. S6c-e, which display the VB intensity, linewidth, and peak position as a function of time (obtained from a fit of the energy distribution curves in Figs. S6a-b). We observe coherent oscillations due to phonon modes, modulating especially the VB linewidth and peak position. Nevertheless, the dynamic changes are too small to be partitioned in the contributions of different phonon modes. To elucidate how each phonon mode contributes to the renormalization of the band structure, we adopt a simplified (*i.e.* adiabatic) computational approach that provides information on the electron-phonon coupling

in the electronic ground state (60). Specifically, we perform G_0W_0 calculations while statically displacing the atoms in the unit cell by 1% (of the interatomic distance) along specific phonon eigenmodes. We remark that this displacement magnitude has been chosen to generate sizable changes in the computed electronic structure. Our results are shown in Fig. S13, where we present the band structure along the Γ-X and Z-M momentum directions for modes I-IV. Note that, to enhance the visibility of the phonon-induced changes, the energy axis is not aligned around E_F, but it is referenced to the energy of infinitely separated atoms. We observe that the low-energy VB states around the Γ point are more sensitive toward the displacement of mode II, in agreement with our results of Fig. 3E. Mode IV leads to an asymmetric and nonlinear behavior of the band structure upon the application of positive and the negative displacements. This behavior occurs in the presence of a non-perturbative strong electron-phonon coupling, which breaks the linear and symmetric dependence expected from the traditional deformation potential theory. Finally, repeating similar calculations at different temperatures (100 K and 300 K) yields no substantial changes in our results. Future studies combining time-resolved X-ray diffraction, trARPES, and advanced calculations will help identify the actual magnitude of the displacement along each particular phonon mode and its distinct effects on the electronic structure of Ta_2NiSe_5 (61).

1. K Okazaki, et al., Photo-induced semimetallic states realised in electron–hole coupled insulators. *Nat. Commun.* **9**, 4322 (2018).
2. T Saha, et al., Photoinduced phase transition and associated timescales in the excitonic insulator ta$_2$nise$_5$. *Phys. Rev. B* **103**, 144304 (2021).
3. QM Liu, et al., Photoinduced multistage phase transitions in ta$_2$nise$_5$. *Nat. Commun.* **12**, 1–8 (2021).
4. C Lee, et al., High resolution time- and angle-resolved photoemission spectroscopy with 11 ev laser pulses. *Rev. Sci. Instrum.* **91**, 043102 (2020).
5. G Kresse, J Hafner, Ab initio molecular dynamics for liquid metals. *Phys. Rev. B* **47**, 558–561 (1993).
6. H Jog, L Harnagea, EJ Mele, R Agarwal, Exchange coupling–mediated broken symmetries in ta$_2$nise$_5$ revealed from quadrupolar circular photogalvanic effect. *Sci. Adv.* **8**, eabl9020 (2022).
7. SA Sunshine, JA Ibers, Structure and physical properties of the new layered ternary chalcogenides tantalum nickel sulfide (Ta_2NiS_5) and tantalum nickel selenide (Ta_2NiSe_5). *Inorg. Chem.* **24**, 3611–3614 (1985).
8. A Nakano, et al., Antiferroelectric distortion with anomalous phonon softening in the excitonic insulator Ta_2NiSe_5. *Phys. Rev. B* **98**, 045139 (2018).
9. A Subedi, Orthorhombic-to-monoclinic transition in $\mathrm{ta_2nise_5}$ due to a zone-center optical phonon instability. *Phys. Rev. Mater.* **4**, 083601 (2020).
10. JP Perdew, K Burke, M Ernzerhof, Generalized gradient approximation made simple. *Phys. Rev. Lett.* (1996).
11. A Togo, I Tanaka, First principles phonon calculations in materials science. *Scr. Mater.* **108**, 1–5 (2015).
12. Z He, AJ Millis, Photoinduced phase transitions in narrow-gap mott insulators: The case of $\mathrm{vo_2}$. *Phys. Rev. B* **93**, 115126 (2016).
13. M Eckstein, P Werner, Thermalization of a pump-excited Mott insulator. *Phys. Rev. B* **84**, 035122 (2011).
14. T Larkin, et al., Giant Exciton Fano Resonance in Quasi-One-Dimensional Ta_2NiSe_5. *Phys. Rev. B* **95**, 195144 (2017).
15. TI Larkin, Excitonic Fano resonances in Ta_2NiSe_5 and Ta_2NiS_5. *PhD Thesis* (2016).
16. YF Lu, et al., Zero-gap semiconductor to excitonic insulator transition in Ta_2NiSe_5. *Nat. Commun.* **8** (2017).
17. YH Wang, et al., Measurement of intrinsic dirac fermion cooling on the surface of the topological insulator bi 2 se 3 using time-resolved and angle-resolved photoemission spectroscopy. *Phys. Rev. Lett.* **109**, 127401 (2012).
18. S Mor, et al., Ultrafast electronic band gap control in an excitonic insulator. *Phys. Rev. Lett.* **119**, 086401 (2017).
19. D Werdehausen, et al., Coherent order parameter oscillations in the ground state of the excitonic insulator Ta_2NiSe_5. *Sci. Adv.* **4** (2018).
20. S Mor, et al., Inhibition of the photoinduced structural phase transition in the excitonic insulator Ta_2NiSe_5. *Phys. Rev. B* **97**, 115154 (2018).
21. D Werdehausen, et al., Photo-excited Dynamics in the Excitonic Insulator Ta_2NiSe_5. *J. Phys. Cond. Matt.* (2018).
22. T Tang, et al., Non-Coulomb strong electron-hole binding in Ta_2NiSe_5 revealed by time- and angle-resolved photoemission spectroscopy. *Phys. Rev. B* **101**, 235148 (2020).
23. SP Weathersby, et al., Mega-electron-volt ultrafast electron diffraction at SLAC national accelerator laboratory. *Rev. Sci. Instrum.* **86**, 073702 (2015).
24. Y Wakisaka, et al., Photoemission spectroscopy of Ta_2NiSe_5. *J. Superc. Nov. Mag.* **25**, 1231–1234 (2012).
25. MD Watson, et al., Band hybridization at the semimetal-semiconductor transition of Ta_2NiSe_5 enabled by mirror-symmetry breaking. *Phys. Rev. Res.* **2**, 013236 (2020).
26. K Seki, et al., Excitonic Bose-Einstein Condensation in Ta_2NiSe_5 above Room Temperature. *Phys. Rev. B* **90**, 155116 (2014).
27. J Lee, et al., Strong interband interaction in the excitonic insulator phase of Ta_2NiSe_5. *Phys. Rev. B* **99**, 075408 (2019).
28. S Mor, *Fundamental interactions governing the (non-) equilibrium electronic structure in low dimensions*. (Freie Universitaet Berlin (Germany)), (2019).
29. T Suzuki, et al., Detecting electron-phonon coupling during photoinduced phase transition. *Phys. Rev. B* **103**, L121105 (2021).
30. S Mor, M Herzog, C Monney, J Stähler, Ultrafast charge carrier and exciton dynamics in an excitonic insulator probed by time-resolved photoemission spectroscopy. *Prog. Surf. Sci.* p. 100679 (2022).
31. MJ Kim, et al., Phononic soft mode behavior and a strong electronic background across the structural phase transition in the excitonic insulator Ta_2NiSe_5. *Phys. Rev. Res.* **2**, 042039 (2020).
32. G Beni, TM Rice, Theory of electron-hole liquid in semiconductors. *Phys. Rev. B* **18**, 768 (1978).
33. S Hellmann, et al., Time-domain classification of charge-density-wave insulators. *Nat. Commun.* **3**, 1069 (2012).
34. SG Han, ZV Vardeny, KS Wong, OG Symko, G Koren, Femtosecond optical detection of quasiparticle dynamics in high-T_c $YBa_2Cu_3O_{7-\delta}$ superconducting thin films. *Phys. Rev. Lett.* **65**, 2708 (1990).
35. P Kusar, et al., Controlled vaporization of the superconducting condensate in cuprate superconductors by femtosecond photoexcitation. *Phys. Rev. Lett.* **101**, 227001 (2008).
36. L Stojchevska, et al., Mechanisms of nonthermal destruction of the superconducting state and melting of the charge-density-wave state by femtosecond laser pulses. *Phys. Rev. B* **84**, 180507 (2011).
37. S Dal Conte, et al., Snapshots of the retarded interaction of charge carriers with ultrafast fluctuations in cuprates. *Nat. Phys.* **11**, 421–426 (2015).
38. F Boschini, et al., Collapse of superconductivity in cuprates via ultrafast quenching of phase coherence. *Nat. Mater.* **17**, 416–420 (2018).
39. T Larkin, et al., Infrared phonon spectra of quasi-one-dimensional Ta_2NiSe_5 and Ta_2NiS_5. *Phys. Rev. B* **98**, 125113 (2018).
40. TE Stevens, J Kuhl, R Merlin, Coherent Phonon Generation and the Two Stimulated Raman Tensors. *Phys. Rev. B* **65**, 144304 (2002).
41. B Mansart, et al., Coupling of a high-energy excitation to superconducting quasiparticles in a cuprate from coherent charge fluctuation spectroscopy. *Proc. Natl. Acad. Sci.* **110**, 4539–4544 (2013).
42. P Hein, et al., Momentum-resolved hot electron dynamics at the 2H-MoS_2 surface. *Phys. Rev. B* **94**, 205406 (2016).
43. F Liu, ME Ziffer, KR Hansen, J Wang, X Zhu, Direct determination of band-gap renormalization in the photoexcited monolayer MoS_2. *Phys. Rev. Lett.* **122**, 246803 (2019).
44. J Yan, et al., Strong electron–phonon coupling in the excitonic insulator Ta_2NiSe_5. *Inorg. Chem.* **58**, 9036–9042 (2019).
45. HM Bretscher, et al., Imaging the coherent propagation of collective modes in the excitonic insulator ta$_2$nise$_5$ at room temperature. *Sci. Adv.* **7**, eabd6147 (2021).
46. K Kim, et al., Direct observation of excitonic instability in ta 2 nise 5. *Nat. Commun.* **12**, 1–8 (2021).
47. PA Volkov, et al., Critical charge fluctuations and emergent coherence in a strongly correlated excitonic insulator. *npj Quantum Mater.* **6**, 1–9 (2021).
48. M Ye, et al., Lattice dynamics of the excitonic insulator ta 2 ni (se 1- x s x) 5. *Phys. Rev. B* **104**, 045102 (2021).
49. A Jain, et al., The Materials Project: A materials genome approach to accelerating materials innovation. *APL Mat.* **1**, 011002 (2013).
50. SP Ong, et al., The materials application programming interface (API): A simple, flexible and efficient API for materials data based on REpresentational state transfer (REST) principles. *Comput. Mater. Sci.* **97**, 209–215 (2015).
51. J Klimeš, DR Bowler, A Michaelides, Chemical accuracy for the van der Waals density functional. *J. Phys. Condens. Matter* **22**, 022201 (2009).
52. J Klimeš, DR Bowler, A Michaelides, Van der Waals density functionals applied to solids. *Phys. Rev. B* **83**, 195131 (2011).
53. T Kaneko, T Toriyama, T Konishi, Y Ohta, Orthorhombic-to-monoclinic phase transition of Ta_2NiSe_5 induced by the Bose-Einstein condensation of excitons. *Phys. Rev. B* (2013).
54. Y Wakisaka, et al., Excitonic insulator state in Ta_2NiSe_5 probed by photoemission spectroscopy. *Phys. Rev. Lett.* **103**, 026402 (2009).
55. L Windgätter, et al., Common microscopic origin of the phase transitions in ta$_2$nis$_5$ and the excitonic insulator candidate ta$_2$nise$_5$. *npj Comput. Mater.* **7**, 1–14 (2021).
56. CD Spataru, LX Benedict, SG Louie, Ab initio calculation of band-gap renormalization in highly excited GaAs. *Phys. Rev. B* **69**, 205204 (2004).
57. L Hedin, New method for calculating the one-particle Green's function with application to the electron-gas problem. *Phys. Rev.* **139**, A796 (1965).
58. M van Schilfgaarde, T Kotani, S Faleev, Quasiparticle self-consistent GW theory. *Phys. Rev. Lett.* **96**, 226402 (2006).
59. S Baroni, P Giannozzi, A Testa, Green's-function approach to linear response in solids. *Phys. Rev. Lett.* **58**, 1861–1864 (1987).
60. E Baldini, et al., Electron–phonon-driven three-dimensional metallicity in an insulating cuprate. *Proc. Natl. Acad. Sci.* **117**, 6409–6416 (2020).
61. S Gerber, et al., Femtosecond electron-phonon lock-in by photoemission and x-ray free-electron laser. *Science* **357**, 71–75 (2017).

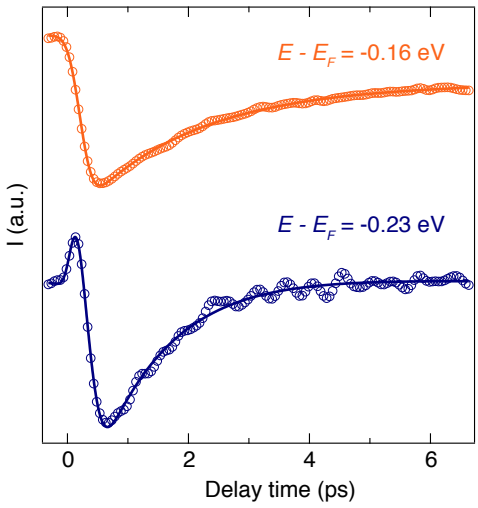

Fig. S1. Temporal traces selected at the energies of -0.16 eV (orange dots) and -0.23 eV (blue dots), referenced to E_F. The solids lines are fit to the data. The overall time resolution can be estimated 160 ± 30 fs, corresponding to the first rise of the trace at -0.23 eV. The data have been acquired at 14 K using the 6.20 eV probe trARPES scheme and an absorbed fluence of 0.85 mJ/cm^2.

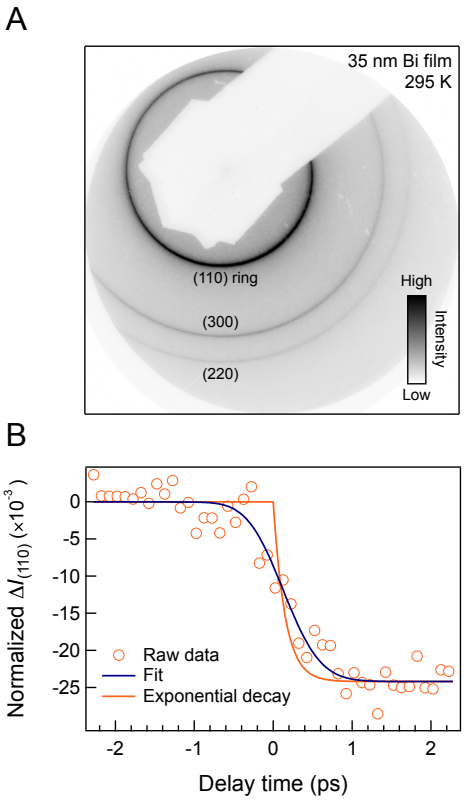

Fig. S2. (A) Static diffraction pattern at room temperature of a 35 nm Bi film, which was deposited on a 10 nm-thick silicon nitride window via electron beam evaporation. The three most prominent Debye-Scherrer rings are labeled. (B) Photoinduced change in the (110) ring intensity, normalized to its value before photoexcitation. Data was taken at 295 K, with a repetition rate of 1 kHz and incident pump fluence of 0.54 mJ/cm^2. Following Ref. (23), the instrumental temporal resolution is determined by fitting the raw data (red circles) with an exponential decaying function (time constant 150 fs, red curve) convolved by a Gaussian kernel. The temporal resolution, 0.8 ± 0.1 ps, is taken as the fitted FWHM of the Gaussian function.

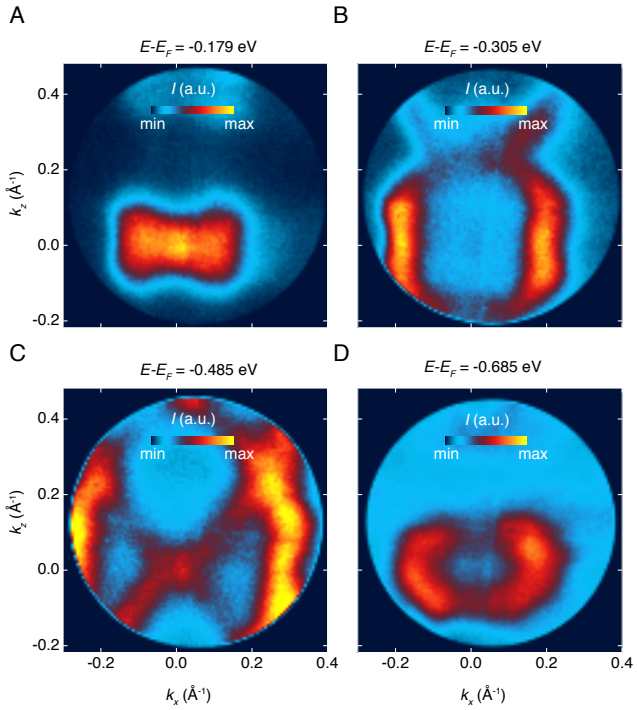

Fig. S3. Constant-energy cuts of the trARPES data at 11 K in the k_x-k_z momentum space, measured before photoexcitation ($t < 0$) with the 10.75 eV probe scheme. Representative energies are referenced to E_F: (A) -0.179 eV; (B) -0.305 eV; (C) -0.485 eV; (D) -0.685 eV.

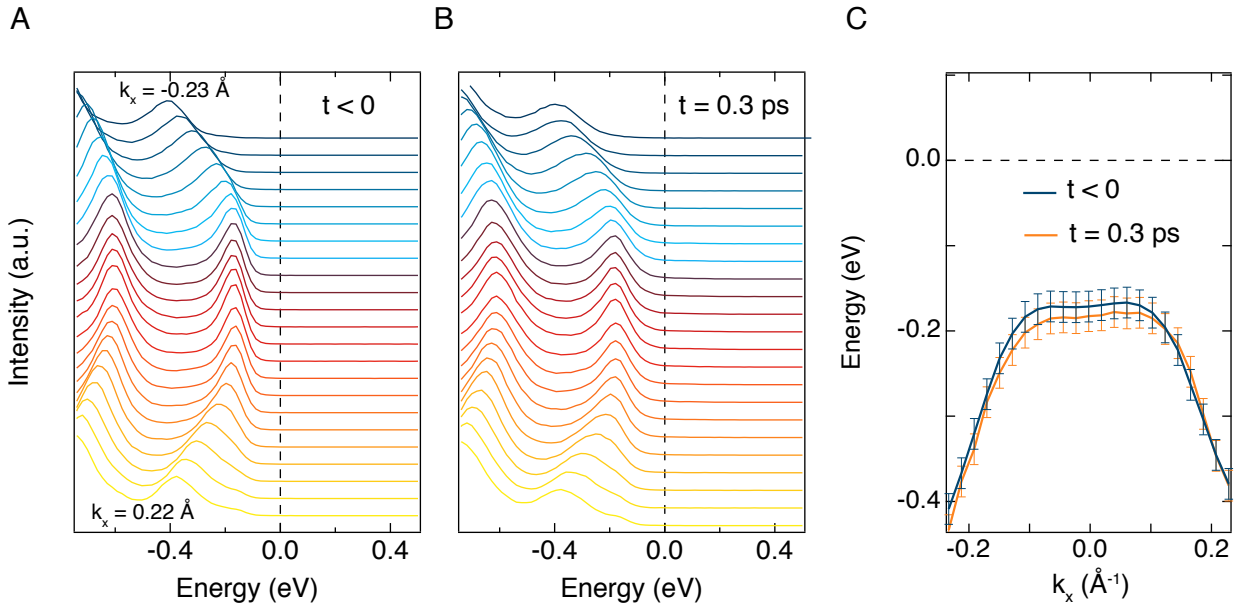

Fig. S4. (A, B), EDCs along k_x, as obtained from the spectra in Figs. 2A, B before time zero and at t = 0.3 ps. (C) Energy-momentum dispersion relation before time zero and at the maximum signal response, as obtained from tracking the VB peak energy at different momenta around the center of the Brillouin zone. The VB peak energy at different momenta has been located by finding the maximum intensity. The error bars have been estimated accounting for the energy spacing between two adjacent data points.

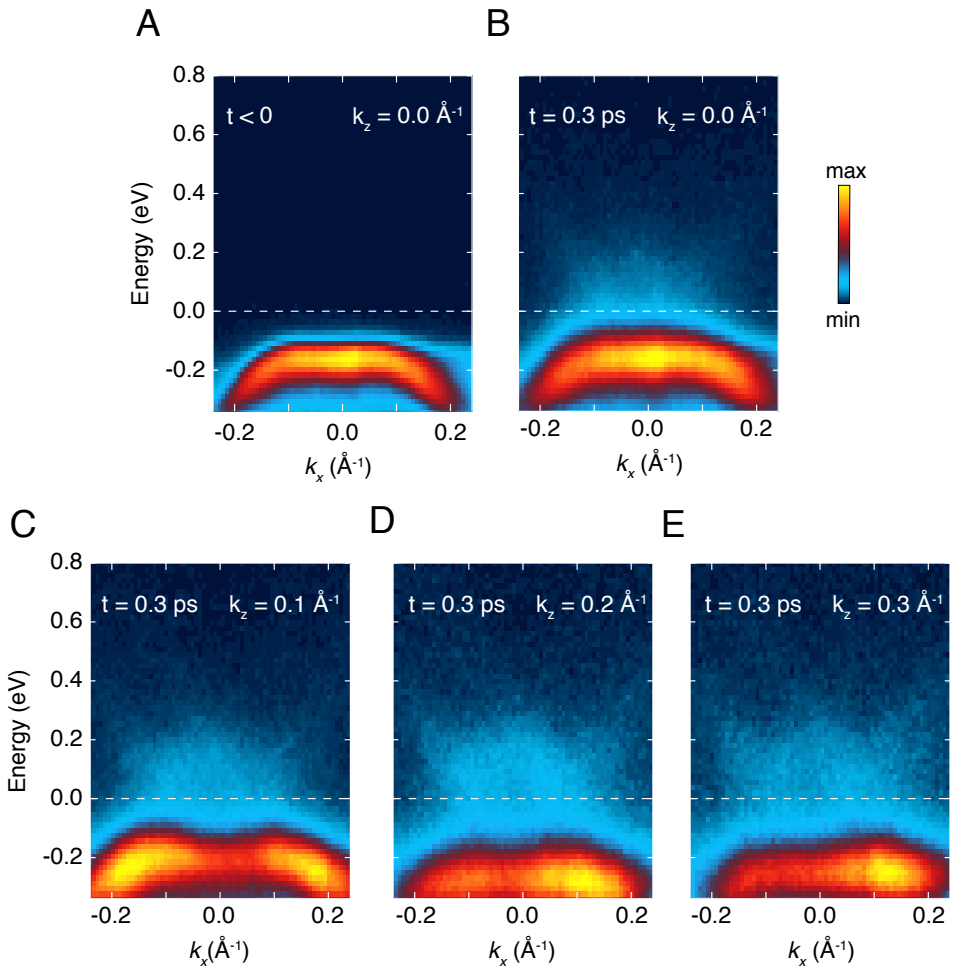

Fig. S5. Snapshots of the trARPES spectra along the k_x momentum direction. (A), Spectrum at $t < 0$ and k_z = 0.0 Å^{-1}. $(B - E)$, Spectra at t = 0.3 ps and for representative k_z momenta, as indicated in the labels. The spectral weight above E_F assumes a W-like shape consistent with the dispersion of the CB. The VB retains its flattened M-like shape. Both features indicate that the hybridization gap is still robust and can be estimated in a range between 180 and 210 meV at k_z = 0.0 Å^{-1}. The snapshots at finite k_z demonstrate that the VB and CB never cross each other in the whole k_x-k_z momentum space around Γ and thus the electronic gap size remains finite. The data have been measured at 11 K with a probe photon energy of 10.75 eV and an absorbed pump fluence of 0.4 mJ/cm^2.

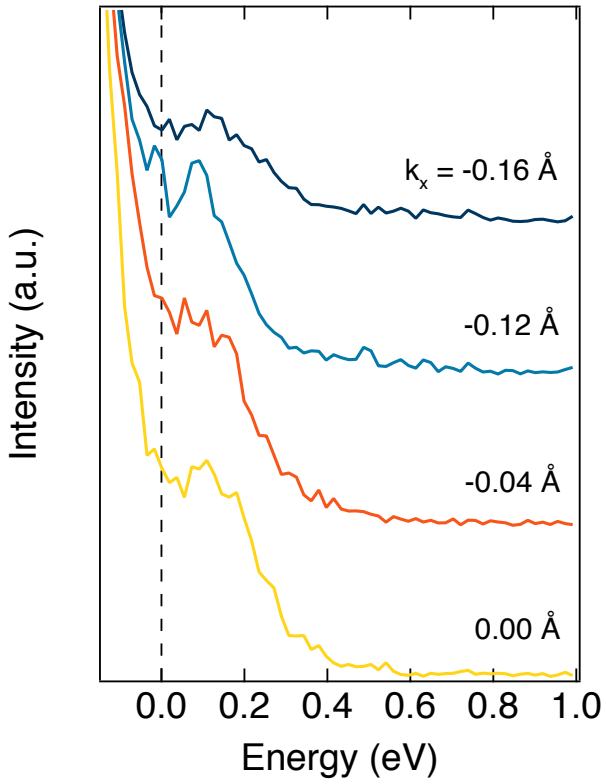

Fig. S6. EDCs along k_x, as obtained at k_z = 0.2Å^{-1} and t = 0.3 ps. The energy axis is resitricted to show the small feature of the CB. Each trace is averaged over a momentum range of 0.024 Å^{-1} around the indicated value.

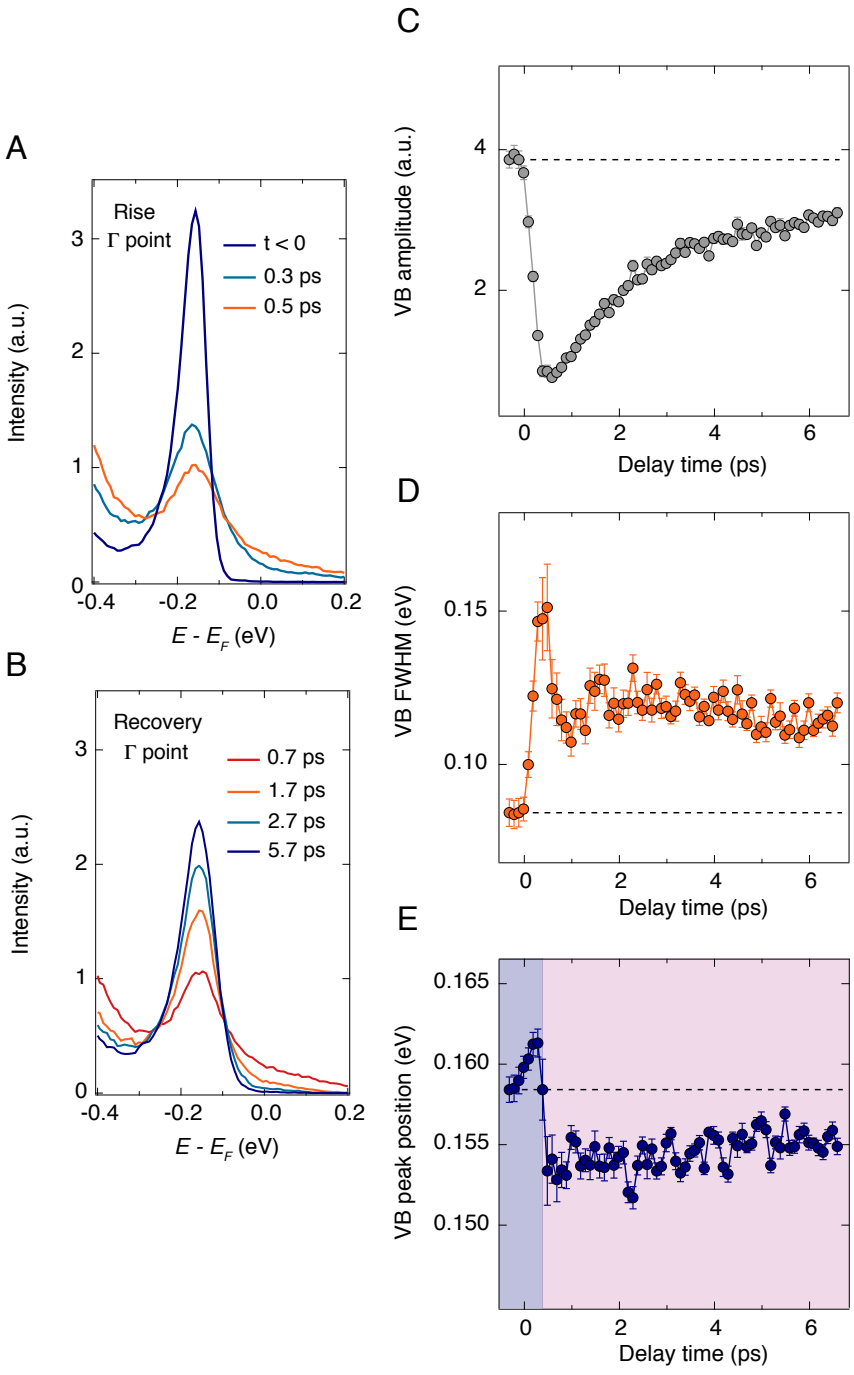

Fig. S7. Time evolution of the EDCs at the Γ point of the Brillouin zone during the (A) rise, and (B) recovery of the response. The data are measured at 14 K with 6.20 eV probe photon energy and an absorbed pump fluence of 0.85 mJ/cm^2. Ultrafast dynamics of the (C) VB amplitude; (D) VB FWHM; and (E) VB peak position. All parameters are extracted from a Lorentz fit to the EDCs.

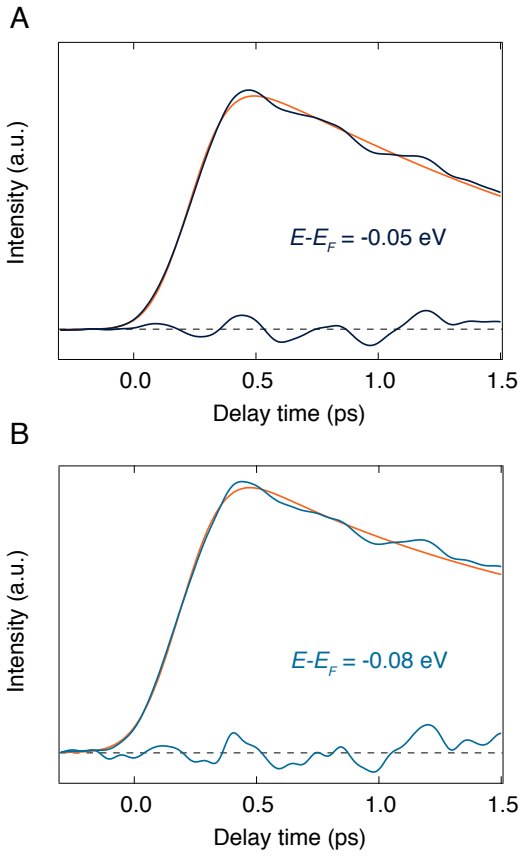

Fig. S8. Time dependence of the momentum-integrated photoelectron intensity around an energy of (A) -0.05 eV and (B) -0.08 eV, referenced to E_F. The energy interval over which the intensity is integrated around the specified energy is $\pm$50 meV. The residual from a multiexponential fit to the data is shown in each panel. The fit function is displayed as an orange curve. For visualization purposes, the data have been smoothed and the residuals have been multiplied by a factor of 2. We observe that the coherent oscillations already appear on the rise of pump-probe responses, suggesting that at least one phonon modes is triggered via an impulsive mechanism (40, 41). In the trace of panel A, all the visible oscillations are real, and the period of the initial cycles is consistent with the 3 THz phonon of Ta_2NiSe_5. In the trace of panel B, the noise floor is slightly higher (because the phonons couple less strongly to this part of the VB), manifesting itself with the residual high-frequency wiggles before time zero and on top of the residuals. However, the 3 THz oscillation starting at t = 0.0 ps can be still clearly distinguished.

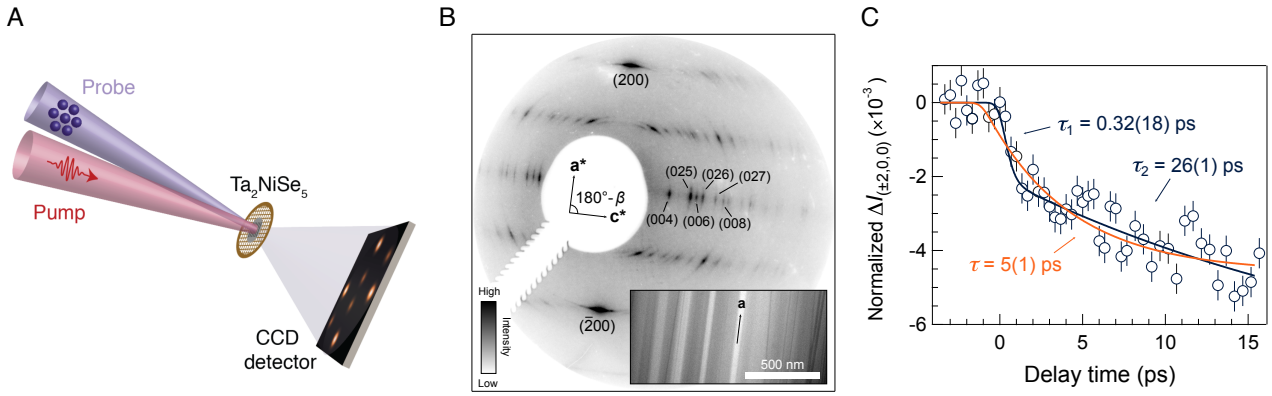

Fig. S9. (A) Schematic of the UED experiment performed in a transmission geometry. An ultrashort near-infrared pump pulse excites the sample and a delayed electron pulse is diffracted by the specimen and captured by a CCD detector. The specimen is in the form of an ultrathin flake deposited on a standard TEM Cu mesh. (B) Static electron diffraction pattern of Ta_2NiSe_5 taken at room temperature and with electrons at an energy of 26 kV. Inset: electron micrograph of the UED sample taken at 120 kV, showing nanoscale needle-like morphology. Though all needles are aligned along the a-axis, their b- and c-axis differ, resulting in peaks observed out of the [010] zone axis; some of these peaks are labeled. (C) Photoinduced change of the integrated diffraction intensity at room temperature, normalized to its value before excitation. The absorbed fluence is 0.1 mJ/cm^2. Intensity values are taken as the average between (200) and $(\bar{2}00)$ peaks. Fit to the temporal trace using a one-exponential decay (orange line) and a two-exponential decay (blue line) functions, both convoluted with a Gaussian function that accounts for the time resolution of the experiment. The extracted timescales are indicated on the figure. Only the use of a two-exponential decay function captures the correct zero time delay of the response and the fast initial decay. Qualitatively similar data were measured at 77 K and 295 K.

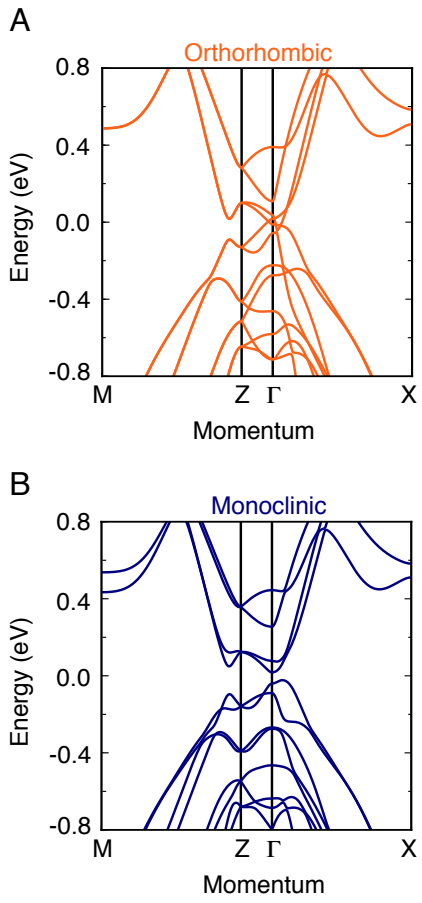

Fig. S10. Electronic structure of Ta_2NiSe_5 calculated on the DFT level by using the PBE functional. (A) The band structure in the orthorhombic lattice symmetry is semimetallic in nature. (B) The band structure in the monoclinic lattice symmetry has a semiconducting character. This indicates that the structural transition alone opens a sizeable bandgap already on the level of standard DFT functionals. A similar effect was found using the modified Becke-Johnson functional.

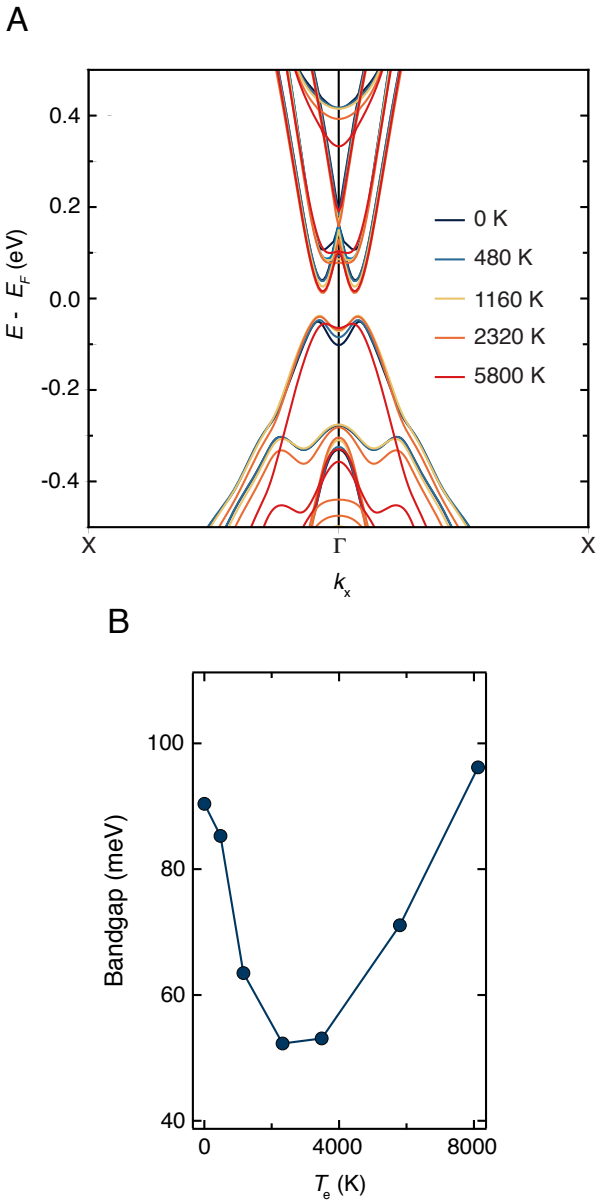

Fig. S11. (A) Electronic structure of Ta_2NiSe_5 calculated on the GW level as a function of T_e (indicated with different color coding as specified in the label). (B) Dependence of the size of the direct bandgap on the T_e. The gap shrinks compared to the equilibrium value for T_e<2500 K and starts to increase from the minimum value reached at T_e>2500 K. This behavior is consistent with the bandgap renormalization known in semiconductor physics (56). The calculations do not account, in principle, for the EI instability.

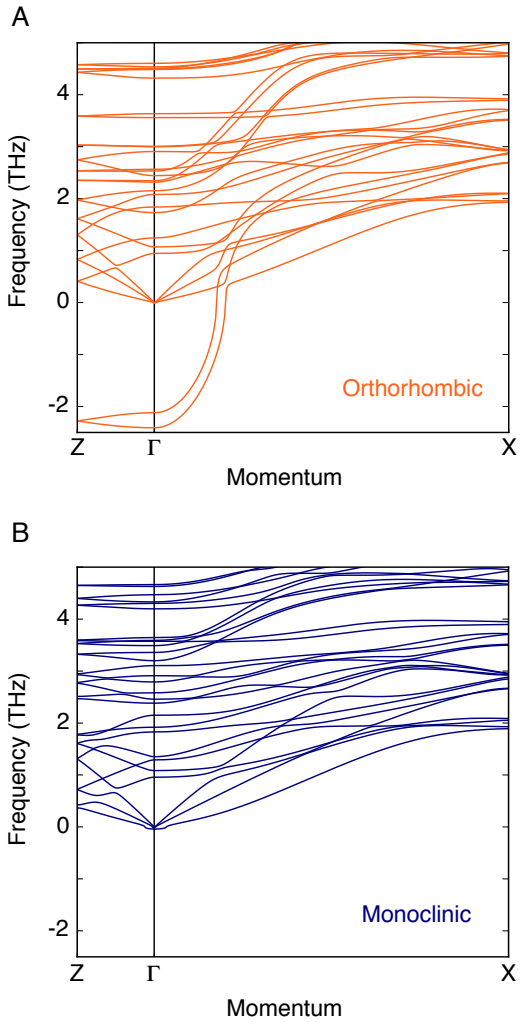

Fig. S12. Phonon energy-momentum dispersion curves calculated in the (A) orthorhombic and (B) monoclinic cell. Two modes acquire a negative (i.e. imaginary) frequency in the orthorhombic structure around the Γ point of the Brillouin zone, which indicates that these phonons are soft modes of the high-temperature unit cell of Ta_2NiSe_5. The modes reappear in the phonon dispersion of the low-temperature monoclinic cell around a frequency of 3.5-4 THz.

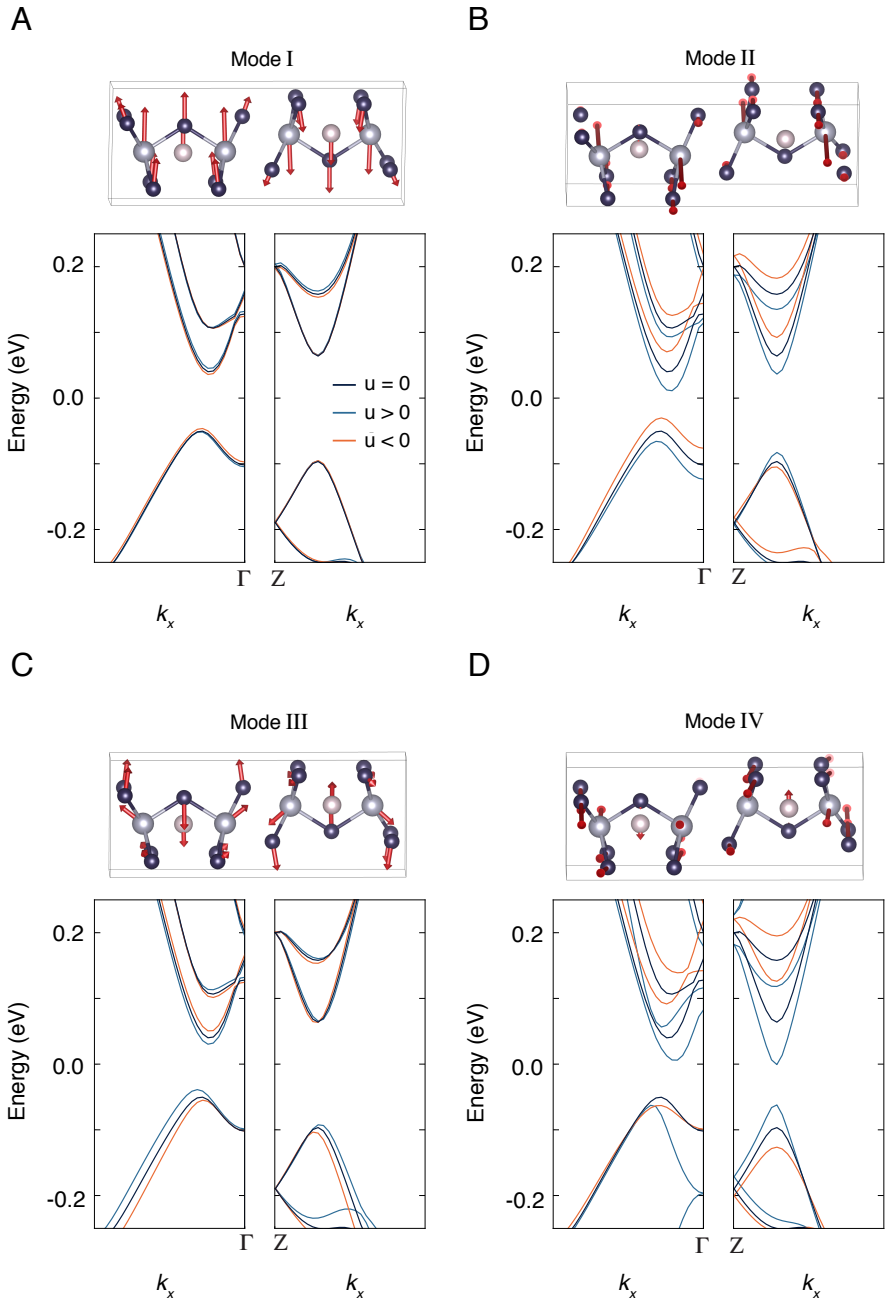

Fig. S13. $(A - D)$, Calculated eigenvectors of the dynamical matrix of Ta_2NiSe_5 corresponding to modes (A) I, (B) II, (C) III, (D) IV of Fig. $3E$. Light-blue atoms refer to Ta, pink atoms to Ni, and dark blue atoms to Se (see the legend in Fig. 4 in the main text). The phonon spectrum has been computed using DFT. To enhance the visibility of the atomic motion, the amplitude is scaled by a factor of 8. The electronic structure of Ta_2NiSe_5 displaced along the eigenvectors of each modes is also shown. The dashed grey lines refer to the electronic structure of the initial (undisplaced) low-temperature unit cell, whereas the orange (blue) solid lines indicate the band structure for positive (negative) displacements. The electronic structures are computed on the GW level of theory.